Catalysis Science & Technology

PAPER

Cite this: *Catal. Sci. Technol.*, 2018, **8**, 858

Methane decomposition to tip and base grown carbon nanotubes and CO_x-free H_2 over mono- and bimetallic 3d transition metal catalysts†

Deepa Ayillath Kutteri,[a] I-Wen Wang,[a] Anupam Samanta,[a] Lili Li*[b] and Jianli Hu *[a]

Received 19th September 2017,
Accepted 1st January 2018

DOI: 10.1039/c7cy01927k

rsc.li/catalysis

Mono- and bimetallic 3d transition metals (Ni, Fe, Co) over a SiO_2 support have been investigated for methane decomposition to CO_x-free H_2 and value added carbon (CNT) in a fixed bed reactor. In our work we synthesized mono/bimetallic Ni, Fe and Co catalysts with various mole ratios. The catalysts were tested under the same reaction conditions for methane decomposition and the influence of their properties on the CNT features was investigated. The synthesized bimetallic catalysts were found to have higher activity and stability than monometallic catalysts. Among the bimetallic catalysts, those with higher Ni content (9Ni–1Fe/SiO_2 and 9Ni–1Co/SiO_2) exhibited higher methane conversion. The properties of fresh and spent catalysts and the CNTs formed were studied using various characterization techniques. XRD and TPR analysis confirmed alloy formation in the bimetallic catalysts. The degrees of graphitization and crystallinity of CNTs formed over various catalysts were calculated using XRD and Raman analysis and were correlated with the catalyst properties. The structural morphology (fishbone or parallel wall type) and growth mechanism (tip or base growth) of the CNTs formed were investigated using TEM analysis. TGA analysis confirmed the absence of amorphous carbon formation during methane decomposition over Ni-, Fe- and Co-based catalysts. We also performed a few preliminary studies to selectively synthesise base grown CNTs over a Fe/SiO_2 catalyst, which are considered to be easier to harvest, and also better for regeneration of catalyst compared to tip grown CNTs.

1. Introduction

Currently hydrogen appears to be an environmentally benign source of energy since it can be converted into electricity and other energy forms with less pollution and high efficiency. Among various methods of hydrogen production, steam reforming of natural gas is the most popular and economical technology, which contributes to 50% of the world's hydrogen consumption.[1] However, these processes are highly endothermic (68.7 kJ mol^{-1} H_2) and produce large amounts of CO_x. As a result, steam reforming is accompanied by the water-gas shift reaction and separation as well as purification steps, thereby increasing the cost of the process. Recently, shale gas has become a very important source of natural gas in the United States. It contributed only 3% of the United States natural gas production in 2005, rising to 35% by 2012 and is predicted to grow to almost 50% by 2035.[2] Increase in demand for CO_x-free hydrogen and the abundance of shale gas resources present opportunities to develop novel chemical processes that convert its major component, methane, into more valuable fuels and chemicals.

Direct decomposition of methane is an attractive alternative process since it is a less endothermic process (37.4 kJ mol^{-1} H_2)[3,4] compared to steam reforming and also has a high H/C ratio compared to other hydrocarbons. This process generates CO_x-free hydrogen, which has a great application in low-temperature fuel cells and also generates valuable carbon nanotubes (CNTs) or nanofibers. In this work we have concentrated more on the production of CNTs from methane. Methane thermally decomposes to atomic carbon, which eventually forms straight and hollow CNTs (R1).

$$CH_4 \leftrightarrow C_{(CNT)} + 2H_2 \quad \text{(R1)}$$

Carbon nanotubes (CNTs) or nanofibers are extensively studied due to their unique physical, chemical, mechanical, electrical and optical properties.[5–8] The applications of CNTs depend on the number of walls, diameter, length, *etc.* which provides them specific properties. They are long graphitic filaments with diameters ranging from 0.4 to 500 nm and lengths from micrometers to millimeters.[9] They can be single

[a] *Chemical & Biomedical Engineering Department, West Virginia University, Morgantown, WV, USA. E-mail: 13672165360@163.com, john.hu@mail.wvu.edu*
[b] *School of Life Science and Agriculture, Zhouko Normal University, Zhouko, Henan, China*

† Electronic supplementary information (ESI) available. See DOI: 10.1039/c7cy01927k

walled or multiwalled. Multiwalled carbon nanotubes (MWCNTs) are predominantly known to have a high surface area and mesoporous structure. These properties increase the application of CNTs as an adsorbent, catalyst support and electrode material. It has been reported that depending on the process conditions, the carbon formed differs, like amorphous (disordered), turbostatic or pyrolytic (less ordered), and carbon filaments (highly ordered, crystalline and graphitic). It is very challenging to produce graphitic carbons (CNTs) by methane decomposition in the absence of a catalyst.[10] Several methods are known for producing high quality carbon nanotubes, such as laser ablation, arc discharge *etc.* These processes have drawbacks like high temperature (1200–3000 °C) and vacuum or low pressure. Non-catalytic decomposition of methane was studied at temperatures of 1000–1100 °C which produced various forms of amorphous carbon.[10] For CNT synthesis, catalysts with nanometer sized metal particles are essential, which will also help to reduce the temperature for methane decomposition.

Many attempts were made to optimize the conditions for the production of CNTs by methane decomposition. Still, these processes are not feasible for industrial-scale production because they are not technically ready. Supported metal catalysts can be used to catalytically decompose hydrocarbons to produce hydrogen at more moderate temperatures. Transition metals like Ni, Fe and Co were widely studied, since their partially filled 3d orbitals facilitate the methane decomposition due to the partial acceptance of electrons from the C–H bond of methane.[11] Among the metal catalysts used, most researchers have focused on Ni-based catalysts due to their high catalytic activity and capability of producing CNTs.[12,13] Although Ni catalysts showed superior performance, they deactivated immediately at temperatures above 600 °C.[14,15] To improve the durability and reduce the deactivation of the catalyst at the reaction temperatures, different metals and metal oxides have been introduced to the Ni-based catalysts.[16–21] Iron-based catalysts have also been studied but showed a shorter lifetime and lower activity than Ni catalysts.[22] When Fe-based catalysts were used, a higher temperature range was also required for an efficient operation. Co catalysts have received less attention than Ni- and Fe-containing catalysts, but still there are few studies which show their activity for methane decomposition.[23–25] Based on previous studies it can summarized that the catalytic activity of iron group metals are in the order Ni > Co > Fe.[24] Unfortunately, the activity of the catalyst is gradually lost during the course of the reaction due to the coverage of active sites by the carbon formed. Recently, it was understood from molecular simulation and experimental results that bimetallic catalysts have a significant influence on the growth properties of CNTs.[26–28]

Bimetallic or alloy catalysts of Ni, Fe or Co will have better stability than monometallic ones due to structural and electronic rearrangements that occur during alloy formation. This property will also help to reduce the activation energy, thereby lowering the CNT growth temperature. Also, these types of catalysts can form stable complexes or solid solutions of small nanoparticles that can prevent their agglomeration, which is followed by the loss in catalytic activity. The growth of CNTs and metal particle size are very much related because metal particle size controls the CNT diameter. Hence it is very important to prepare a catalyst with controlled particle size to grow CNTs with a controlled diameter. A combination of monometallic catalysts with other active metals can lead to some promising catalysts.[16,25,29,30] Hence in our work we have attempted to employ a mixture of two metals to combine their individual advantages. Besides the catalyst material, the catalyst concentration also plays an important role in the CNT growth. Thus, by combining different metals in different ratios and carefully controlling the catalyst calcination conditions, it is possible to evolve new crystallographic phases that could exhibit much higher catalytic activity toward CNT growth.

A majority of the above-mentioned studies have shown that catalytic methane decomposition forms CNTs by "tip growth". One of the main disadvantages of tip grown CNTs is that during the harvesting of CNTs from the catalyst using acid or base treatment the metal nanoparticles are dissolved and the catalyst is sacrificed. Also, for a tip grown CNT, catalyst nanoparticles which are attached to its tip are considered as an impurity. Hence extraction of CNTs with complete recovery of the catalyst is most recommended. To overcome this problem, catalysts and reaction processes were designed in such a way as to produce "base grown" CNTs. Base grown CNTs can be easily harvested and the catalyst can be regenerated without being consumed during the extraction process. In addition, a literature survey has shown that very little amount of research was done in the area of base grown CNTs and their advantages over tip grown CNTs. Hence a portion of our research is also focused on the synthesis of base grown CNTs. There are only very few reports which show the base growth study of CNTs. The base-growth mechanism was reported for MWCNTs[31,32] and also for SWCNTs.[31,33] One of the methods employed was chemical vapour deposition (CVD) with ethylene as the carbon source and iron oxide on porous Si as the catalyst.[34] Iron oxide nanoparticles remain attached to the support during CVD growth, and thus base growth occurs. Still, it remains unclear how to scale up these processes because of the lack of strategies in scaling up nanotube growth. Another report shows the growth process of carbon nanotubes (CNTs) from iron carbide (Fe_3C) nanoparticles in chemical vapour deposition with ethylene.[31] Based on the previous literature we have to incorporate the metal–support interaction concept for base growth CNT synthesis using Fe/SiO_2 catalysts in methane decomposition reactions.

To summarize, there are only very few studies that have correlated the catalyst properties (Ni, Fe or Co-based catalysts) with the properties of CNTs formed during methane decomposition. Most of the literature cited has studied these metals individually as catalysts for CNT formation and H_2 production. Also, in the existing literature there a lack of

information on how different metals affect the physical and chemical properties of as-grown CNTs. Through our research we have tried to draw a correlation between the properties of CNTs and the type of metal used, which would help us to grow CNTs with significant selective properties. Also we have explored the synthesis of base grown CNTs using monometallic catalysts. The advantages of base grown CNTs are that they can be easily harvested and help in better regeneration of the catalyst. Thus, the present work aims to prepare catalysts and also investigate the relation between the catalyst properties and the properties of carbon nanomaterials, both tip and base grown CNTs, along with CO_x-free hydrogen by methane decomposition.

2. Experimental section

2.1. Catalyst preparation and characterization

Mono- and bimetallic Ni, Fe, and Co catalysts were prepared by a dry impregnation or incipient wetness impregnation method. $Ni(NO_3)_2{\cdot}6H_2O$ (Acros Organics), $Fe(NO_3)_2{\cdot}9H_2O$ (Alfa-Aesar) and $Co(NO_3)_2{\cdot}6H_2O$ (Acros Organics) were used as precursors. Fumed SiO_2 (CAB-O-SIL-EH-5 untreated SiO_2, CABOT) was used as support material. An aqueous solution of metal precursor (corresponding to 60 wt% metal loading) was impregnated into the support (40 wt%). The sample was dried in an oven at 130 °C overnight (16 h). This as-synthesized catalyst was subjected to calcination in a muffle furnace and then reduced in 10% H_2 in an Ar flow (70 ml min^{-1}). Monometallic Ni/SiO_2 was calcined at 500 °C, 5 °C min^{-1} for 10 h and reduced at 450 °C, 10 °C min^{-1} for 4 h; Fe/SiO_2 was calcined at 500 °C, 5 °C min^{-1} for 10 h and reduced at 700 °C, 10 °C min^{-1} for 4 h; Co/SiO_2 was calcined at 450 °C, 5 °C min^{-1} for 3 h and reduced at 580 °C, 10 °C min^{-1} for 4 h. Bimetallic $Ni–Fe/SiO_2$ was calcined at 500 °C, 5 °C min^{-1} for 10 h and reduced at 700 °C, 10 °C min^{-1} for 4 h; $Ni–Co/SiO_2$ was calcined at 750 °C, 5 °C min^{-1} for 5 h and reduced at 700 °C, 10 °C min^{-1} for 2 h; $Fe–Co/SiO_2$ was calcined at 450 °C, 5 °C min^{-1} for 3 h, and reduced at 580 °C, 10 °C min^{-1} for 4 h. The present work concerns monometallic Ni, Fe, and Co and bimetallic Ni–Fe, Ni–Co and Fe–Co catalysts. Bimetallic catalysts were prepared by a co-impregnation method with different mole ratios such as 1 : 1, 1 : 2, 2 : 1, 9 : 1, 4 : 1, and 1 : 9. Catalysts are denoted as *x*M–*y*N, where M, N and *x*, *y* stand for metal and mole number, respectively. Details on catalyst compositions are included in Table S1† in the ESI.

Catalyst characterization was performed using the following techniques. Temperature programmed reduction (TPR) was performed for the catalysts using a Micromeritics AutoChem HP chemisorption analyser equipped with a TCD detector. The catalysts were degassed in He at 200 °C for 1 h. After cooling to RT, the temperature was ramped to 850 °C in 10 vol% H_2/Ar (50 ml min^{-1}) with a linear heating rate of 10 °C min^{-1} and the TCD signal was recorded. Catalysts with carbon deposition obtained after reaction at 700 °C were characterized by X-ray diffraction (XRD). XRD measurements were performed on a PANalytical X'pert Pro diffractometer using Cu Kα radiation. The step scans were taken over the range of 10–90° and the scan rate was 5° min^{-1}. The morphologies and microstructures of the carbon materials were characterized by transmission electron microscopy (TEM) using a JEOL TEM-2100 instrument. The samples were prepared by sonication of the spent catalyst in isopropanol and the suspension was dropped onto a Cu-TEM grid for analysis. Raman experiments were performed using a Renishaw inVia Raman spectrometer at ambient atmosphere and room temperature. Spectra were recorded using a green excitation line at 532 nm. Thermogravimetric analysis was performed using a TA_SDT-650_Discovery model instrument in a 5% O_2/He atmosphere, from 150–700 °C, at a heating rate of 2 °C min^{-1}.

2.2. Reactor apparatus

Catalytic methane decomposition was performed in a fixed-bed flow reactor (10 mm i.d. and 44.5 cm long quartz tube) at atmospheric pressure. In a typical test, 0.1 g catalyst was placed in the reactor bed and the reaction temperature was measured with a K-type thermocouple fixed at the catalyst bed. Prior to activity tests, the catalysts were subjected to reduction at their respective temperatures and were later purged with N_2 for 30 min. Then the temperature was increased to 650 °C (10 °C min^{-1}) in N_2 (70 ml min^{-1}) and the feed was switched to reactant gas (30% CH_4/N_2, 70 ml min^{-1}) and a space velocity of 42 000 h^{-1} was achieved. The composition of the outlet gas was determined with an online gas chromatograph (Perkin ElmerARNEL, Clarus 500) equipped with a thermal conductivity detector with HayeSep N 60/80, HayeSep T 60/80, Molecular Sieve 5A 45/60, and Molecular Sieve 13× 45/60 packed columns. The GC data were processed using TotalChrom Workstation software. GC was well calibrated with standard gases before analysis. Catalyst reproducibility was tested and the results were with ±5% error.

3. Results and discussion

The activity of supported metal catalysts relies on the shape, size, distribution and degree of agglomeration of the metal particles or the active sites on the support. Hence the physicochemical properties of the catalysts were studied before and after the reaction. After the methane decomposition reaction (1 h), the used catalysts were dried at 120 °C for 2 h and characterized. The CNT formed was deposited on the catalyst and was also characterized using several characterization techniques.

3.1. Properties of fresh, spent mono- and bimetallic supported metal catalysts

Catalyst properties were investigated using XRD and TPR techniques (ESI†). The characteristic peaks for all the metals (Ni, Fe and Co) were identified using XRD analysis (Fig. S1–S6, ESI†). The amorphous peak of the SiO_2 support was not

visible in the diffractogram due to high intense peaks for the metal loaded (60% metal on 40% SiO_2 support). The sharp peaks for metals confirmed the crystalline phase of the active element (Ni/Fe/Co) and the corresponding 2θ values represented their metallic state. Ni characteristic peaks were observed at $2\theta^o$ = 44.6°, 52.0°, and 76.6° (JCPDS no. 04-850); Fe characteristic peaks were at $2\theta^o$ = 45.1°, 65.5°, and 82.8° (JCPDS no. 65-4899) and for Co the peaks were at $2\theta^o$ = 44.4°, 51.6°, and 76° (JCPDS no. 15-0806). For bimetallic Ni–Fe catalysts with different ratios, we observed a peak shifting which signified alloy formation (Fig. S1(b)†). The transformation from the fcc to the bcc phase as a function of Fe content was observed in Ni–Fe bulk alloys.[35,36] For the monometallic Ni catalyst the (111) plane represents the fcc phase and for the monometallic Fe catalyst the (110) plane represents the bcc phase. In the bimetallic catalyst, when Fe is introduced to a Ni-rich system (9Ni–1Fe) a single set of diffraction patterns corresponding to the fcc phase of Ni–Fe alloy was observed. This peak was also found to be shifted towards a lower 2θ value, converging to the diffraction pattern of the Ni fcc phase. Similarly for the Ni–Co bimetallic catalyst, alloy formation was confirmed using XRD analysis (Fig. S3, ESI†). The fcc phase (111) of monometallic Co was observed at 2θ = 44.4°, which was slightly shifted towards a higher 2θ value (Ni phase), representing the Ni–Co alloy formation. Also for the Fe–Co bimetallic system, alloy formation was observed where the bcc phase for Fe was shifted towards the lower 2θ values, representing the fcc phase of Co and the Fe–Co alloy formation (Fig. S5, ESI†). Hence from XRD analysis, we could confirm the formation of alloy in the bimetallic Ni/Fe/Co catalysts prepared, which thereby would help to increase the stability of the catalyst under the reaction conditions.

After the reaction the used catalysts were once again characterized by XRD analysis (Fig. S2, S4 and S6, ESI†). The majority of the catalysts were stable in their metallic form but the monometallic Fe catalyst (Fig. S2, ESI†) has undergone oxidation, which was very obvious as Fe is prone to oxidation when exposed to air. However, for the bimetallic catalysts, it was observed that the alloy formation has helped to prevent the oxidation of the metals thereby increasing their lifetime or stability. From the XRD data the average crystallite size of metal nanoparticles before and after the reaction was calculated using the Scherrer equation (Table S1, ESI†). When bimetallic catalysts were prepared, we could observe a significant decrease in the crystallite size. Hence bimetallic catalysts prevent the agglomeration of the nanoparticles, which signifies the stable nature of the catalyst. Strangely, for the monometallic Fe catalyst, the crystallite size was decreased (29 nm to 13 nm) which could be because a portion of Fe sites was being oxidised to iron oxides when exposed to air.

To investigate the reducibility of the synthesized catalysts, H_2-TPR experiments were conducted and the results are shown in Fig. S7–S9 (ESI†). The TPR results also support the XRD data for the alloy formation in the bimetallic catalysts. In the monometallic Ni catalyst, two reduction peaks were observed, one at around 367 °C and the other at 470 °C (Fig. S7, ESI†). The first peak corresponds to the reduction of bulk NiO, which weakly interacted with the SiO_2 support, and the second weak reduction peak was for the reduction of NiO species, which had a very strong interaction with the SiO_2 support.[37] For monometallic Fe catalyst, a typical TPR profile has three peaks at around 470, 576 and 727 °C, respectively (Fig. S7, ESI†). These correspond to the three consecutive reduction steps, α-Fe_2O_3 → Fe_3O_4 → FeO → Fe.[38,39] In the monometallic Co catalyst the low temperature reduction peak centered at 306 °C and the second peak at 360 °C was assigned to the two-step reduction of spinel, *i.e.*, Co_3O_4 → CoO → Co (Fig. S8, ESI†). An additional shoulder peak was also observed at around 433 °C.[40] However, the absence of high reduction temperature peaks shows that the interaction of cobalt with the SiO_2 support was not strong. TPR studies of bimetallic Ni–Fe catalysts showed that with the increase in Ni content the high temperature reduction peaks of Fe were shifted towards the reduction temperature of Ni species (Fig. S7, ESI†). For Fe–Co catalysts, the increase in Co content lowered the reduction temperature of the catalyst or Co facilitated the reduction of Fe (Fig. S9, ESI†). When Fe was present in high concentrations, the catalyst exhibited the properties of Fe. Hence an increase in the Co reduction temperature was observed.[41,42] The TPR profiles of Ni–Co catalysts (Fig. S8, ESI†) indicated that Co_3O_4 was easier to reduce than NiO, whereas an increase in Ni content retards the reduction of Co_3O_4. Hence the incorporation of Co should improve the reducibility of NiO.

3.2. Effect of catalyst composition on methane decomposition and CNT growth

3.2.1. Ni–Fe bimetallic catalysts. Initial studies were performed using monometallic Ni/SiO_2 catalyst. It was observed that even though Ni/SiO_2 showed a high CH_4 conversion of 50%, it started deactivating and reached a conversion of 40% in 60 min of reaction (Fig. 1). Similarly, monometallic Fe/SiO_2 was tested, which showed a very low initial activity of 11% and gradually deactivated to 4% CH_4 conversion. Monometallic Ni/SiO_2 was a very active catalyst; unfortunately, it

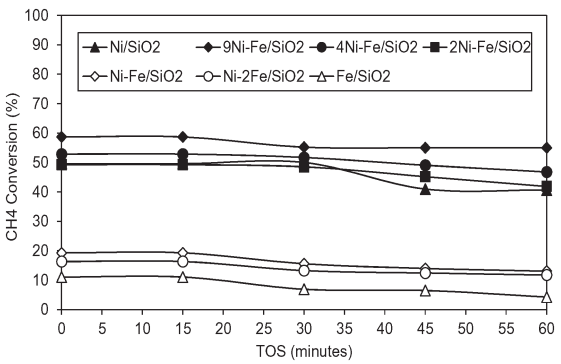

Fig. 1 Methane decomposition over Ni–Fe/SiO_2 catalysts with various mole ratios at T = 650 °C, TOS = 0–60 minutes, GHSV = 42 000 h^{-1}.

deactivated very fast. Hence the effect of Fe promoter addition on the activity of the Ni/SiO_2 catalyst for methane decomposition reaction has been shown. Several Ni–Fe mole ratios (9 : 1, 4 : 1, 2 : 1, 1 : 1, 1 : 2) were studied. $4Ni–1Fe/SiO_2$ and $2Ni–1Fe/SiO_2$ exhibited a similar activity (~50% CH_4 conversion) to monometallic Ni/SiO_2 catalyst at TOS = 30 min., but afterwards it was observed that $4Ni–1Fe/SiO_2$ catalyst retained its activity even after TOS = 60 min, whereas $2Ni–1Fe/SiO_2$ deactivated like the Ni/SiO_2 catalyst. Reactions were also performed with $1Ni–1Fe/SiO_2$ and $1Ni–2Fe/SiO_2$, which showed a very low CH_4 conversion (16–20%) compared to the above catalysts, but they had maintained the activity throughout the reaction time. Thus it was concluded that high Ni content in the Ni–Fe bimetallic catalyst exhibits higher conversion, which helps to increase the stability or the lifetime of the catalyst. Hence $9Ni–1Fe/SiO_2$ was prepared, which showed an excellent conversion rate of 60%, the highest among all the Ni and Fe catalysts studied here, and its activity was very stable even at 60 min of reaction. The H_2 yield was found to be in the range of 30–40% for catalysts with higher Ni content such as $9Ni–1Fe/SiO_2$, $4Ni–1Fe/SiO_2$, and $2Ni–1Fe/SiO_2$, while the rest of the catalysts showed only 5–12% H_2 yield (Fig. S10, ESI†). The amount of carbon formed per gram of catalyst was calculated, which was found to be approximately 2.3–2.5 g over $9Ni–1Fe/SiO_2$, $4Ni–1Fe/SiO_2$, and $2Ni–1Fe/SiO_2$ and was less than 0.4 g for the rest of the catalysts (Fig. S11, ESI†).

3.2.2. Ni–Co bimetallic catalysts. Methane conversion over mono- and bimetallic Ni and Co catalysts are studied in this section. Under the reaction conditions Co/SiO_2 showed a CH_4 conversion of 37%, but deactivated to 9% within 5 min of reaction (Fig. 2). Ni/SiO_2 already showed good initial activity but had a gradual deactivation during the course of the reaction. Hence, to improve the activity of Co/SiO_2 and to increase the stability of Ni/SiO_2 catalysts, we have prepared a bimetallic combination of Ni–Co catalysts with various Ni : Co mole ratios, such as 9Ni–1Co, 4Ni–1Co, 2Ni–1Co, 1Ni–1Co, 2Ni–1Co, and 1Ni–9Co, on a SiO_2 support. Similar to Ni–Fe catalysts, the Ni–Co combination also showed a maximum conversion of 55%. Ni–Co catalysts such as 9Ni–1Co, 4Ni–1Co, 2Ni–1Co, and 1Ni–1Co showed a similar initial conversion of 50–55% and retained their activity throughout the reaction. A catalyst with higher Co content was also tested, 1Ni–9Co, which showed an initial conversion of 53%, but within 15 minutes of reaction. It was observed that the high Ni content in the Ni–Co bimetallic catalyst exhibited higher conversion and the presence of Co as a promoter contributed to increasing the catalyst lifetime.

H_2 yield was found to be in the range of 38–40% for catalysts with higher Ni content such as $9Ni–1Co/SiO_2$, $4Ni–1Co/SiO_2$, and $2Ni–1Co/SiO_2$, whereas Co/SiO_2 and $1Ni–9Co/SiO_2$ showed only an initial H_2 yield of 28–33% which reduced to 6% within 5 min of reaction (Fig. S12, ESI†). The amount of carbon formed per gram of catalyst was calculated, which was found to be approximately 2.3–2.5 g over $9Ni–1Co/SiO_2$, $4Ni–1Co/SiO_2$, and $2Ni–1Fe/SiO_2$ and was 0.15–0.27 g for Co/SiO_2 and $1Ni–9Co/SiO_2$ catalysts (Fig. S13, ESI†).

3.2.3. Fe–Co bimetallic catalysts. Methane decomposition reactions over mono- and bimetallic Fe–Co catalysts are explained in this section (Fig. 3). Bimetallic $Fe–Co/SiO_2$ catalysts were prepared with various Fe : Co mole ratios, such as 9Fe–1Co, 2Fe–1Co, 1Fe–1Co, 1Fe–2Co, and 1Fe–9Co, over a SiO_2 support. It was observed that $1Fe–2Co/SiO_2$ showed the highest CH_4 conversion of 51% but has undergone drastic deactivation and showed a conversion of only 15% at 60 min of reaction. Among the catalysts studied here, even though the activity is not excellent, the stability was better over $9Fe–1Co/SiO_2$ and $4Fe–1Co/SiO_2$. Maximum H_2 yield of 29% (Fig. S14, ESI†) and carbon yield of 0.8 g was observed with $1Fe–2Co/SiO_2$ (Fig. S15, ESI†).

3.3. Comparison of activities of reduced and oxidised catalysts

Generally, transition metal catalysts (Ni/Fe/Co) were used in their reduced forms ($Ni^0/Fe^0/Co^0$) for the CNT synthesis by methane decomposition. However, some literature reports have shown that it may not be necessary to pre-reduce the

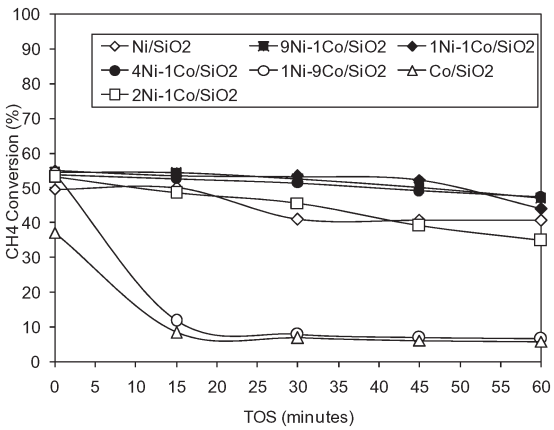

Fig. 2 Methane decomposition over $Ni–Co/SiO_2$ catalysts with various mole ratios at T = 650 °C, TOS = 0–60 minutes, GHSV = 42 000 h^{-1}.

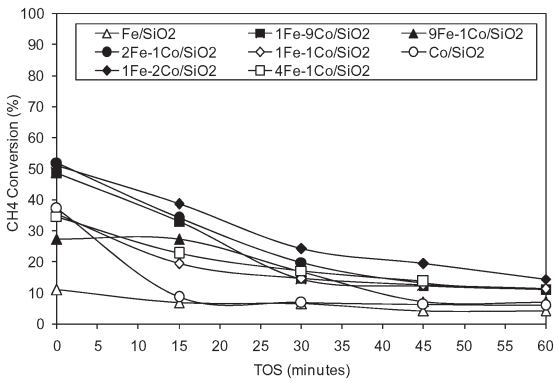

Fig. 3 Methane decomposition over $Fe–Co/SiO_2$ catalysts with various mole ratios at T = 650 °C, TOS = 0–60 minutes, GHSV = 42 000 h^{-1}.

catalysts for the reaction.[43] For our experiments we have used oxidised and reduced forms of 9Ni–1Fe/SiO_2 catalyst since it has shown a very good activity for methane decomposition reactions (Fig. S16, ESI†). Both the catalysts showed a similar activity at the initial point of the reaction (*ca.* 60%). The activity shown by the oxidised catalyst can be due to the *in situ* reduction of the lattice oxygen which supplied energy for methane decomposition, which is an endothermic process. In addition, there can be an *in situ* consumption of H_2 formed, which assisted the shifting of the equilibrium towards the methane decomposition step or carbon formation.[43] As we have shown before (Fig. 1), the reduced 9Ni–1Fe/SiO_2 catalyst showed a constant activity till the end of the reaction but the oxidised form of the catalyst was gradually deactivated from 60% to 41% conversion rate in 60 min of reaction time. The amount of carbon formed per gram of catalyst was also in the range of 2.2–2.5 g for both catalysts. In summary, in our case even though the oxidised form of the catalyst catalysed the methane decomposition to carbon and H_2, the stability of the catalysts was lesser compared to that of their reduced forms. This may be because reduced forms are stabilised due to their alloy phases, which helps to increase their lifetime and stability.

3.4. Properties of CNTs

The CNTs formed by catalytic methane decomposition were characterized by XRD, TG, Raman and TEM analysis.

3.4.1. XRD analysis. All the XRD patterns of the used catalysts showed the presence of graphitic carbon by a very intense peak (002) at $2\theta = 26.2°$ (Fig. S2, S4 and S6, ESI†).

All characteristic metal and alloy peaks were also identified; however we could not observe any metal carbide formation in these catalysts. From the XRD pattern it is difficult to differentiate the microstructural features between CNT and similar graphitic structures since their characteristic peaks are overlapped.[44] Furthermore, the *d*-spacing of CNTs was calculated using Bragg's equation ($d = \lambda/2\sin\theta$) for the graphitic peak, which was found to be 0.34 nm, and it correlates well with the distance of two graphite layers (0.3354 nm), implying the high crystallinity of the carbon grown over all the catalysts. The intensity of the (002) diffraction peak is related to the degree of graphitization (Fig. 4). Thus, a lower intensity represents the less graphitized material.[45] In the case of Ni–Fe bimetallic catalysts, we can observe that 9Ni–1Fe/SiO_2 or the bimetallic catalyst with the highest Ni content produced CNTs with the highest degree of graphitization and the degree decreases with an increase in the amount of Fe in the catalyst.

The degree of graphitization for Ni–Fe catalyst was in the order 9Ni–1Fe > Ni > 4Ni–1Fe > 2Ni–1Fe > 1Ni–2Fe > Fe. For Ni–Co bimetallic catalyst, 4Ni–1Co/SiO_2 produced CNTs with the highest graphitization degree in the order 4Ni–1Co > 2Ni–1Co > Ni > 1Ni–1Co = 9Ni–1Co > 1Ni–9Co > Co. For Fe–Co catalysts the overall intensity of the CNT peak was very low compared to Ni-based catalysts and the whole set of Fe–Co catalysts produced less graphitized CNT. Hence, in general the Ni content in the bimetallic catalyst is influencing the degree of graphitization of the carbon formed during the methane decomposition reaction.

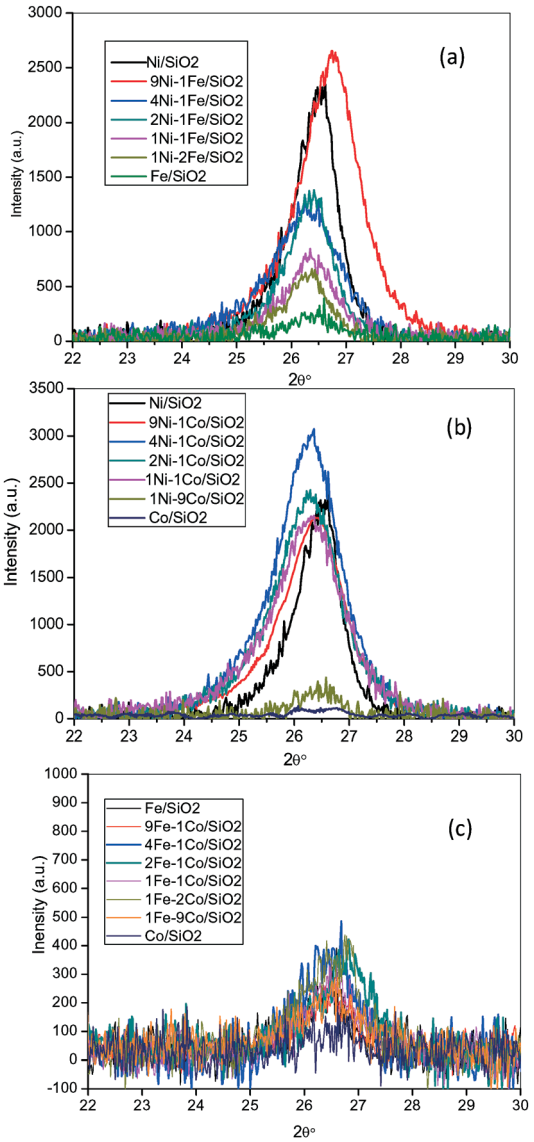

Fig. 4 XRD pattern of CNT over mono- and bimetallic (a) Ni–Fe (b) Ni–Co and (c) Fe–Co catalysts.

3.4.2. Thermogravimetric analysis (TGA). The thermal stability of CNT was studied using thermogravimetric analysis. The catalysts 9Ni–1Fe/SiO_2, 9Ni–1Co/SiO_2 and 1Fe–2Co/SiO_2 were studied, since these catalysts showed better activity than the rest of the catalysts (Fig. 5). These catalysts were analysed in a 2%O_2/He atmosphere. The carbon deposited on the catalyst, amorphous or CNT, decomposes into CO or CO_2 in an O_2 atmosphere. In certain cases there is a possibility that the catalyst species are also oxidized under these conditions. It was observed that there was no thermal degradation in the temperature range of 200–350 °C, which corresponds to amorphous carbon. Hence we could confirm that the carbon

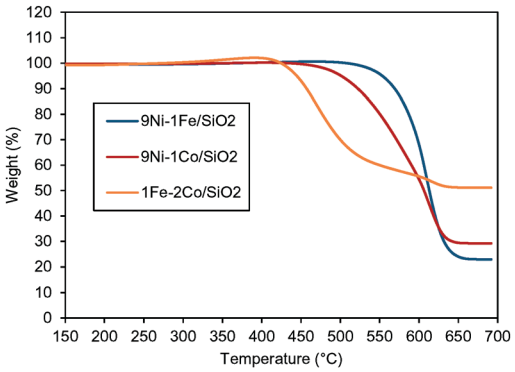

Fig. 5 Thermal stability of carbon deposited over 9Ni–1Fe/SiO_2, 9Ni–1Co/SiO_2 and 1Fe–2Co/SiO_2 catalysts.

deposited on these catalysts is not amorphous in nature. The weight loss observed in all these catalyst corresponds to the CNT deposited on the catalyst. From TGA analysis of CNTs it is understood that the higher the degradation temperature of carbon, the higher its stability. For 9Ni–1Fe/SiO_2, the thermal degradation started at around 500 °C and there was a weight loss of 75%. For 9Ni–1Co/SiO_2, degradation started from 450 °C with a weight loss of 70%. For 1Fe–2Co/SiO_2 catalyst, there was a slight increase (2%) in weight at a temperature of around 350 °C, which can be due to the oxidation of Fe present in the catalyst. At around 410 °C, a weight loss of 45–50% was observed, which was lower than that of 9Ni–1Fe/SiO_2 and 9Ni–Co/SiO_2 catalysts. The onset temperatures for 9Ni–1Fe/SiO_2, 9Ni–Co/SiO_2 and 1Fe–2Co/SiO_2 are 500–660 °C, 450–650 °C and 410–640 °C, respectively, which indicates that the CNT formed over 9Ni–1Fe/SiO_2 catalyst has a higher degree of graphitization as well as lesser defects on the CNTs.[46] Hence it can be concluded that the smaller difference in the onset and end temperatures indicates the formation of highly graphitized CNTs. It is also understood that there is no amorphous carbon formation during methane decomposition over these catalysts and the amount of carbon formed over 1Fe–2Co/SiO_2 is the minimum in comparison to 9Ni–1Fe/SiO_2 and 9Ni–Co/SiO_2 catalysts.

3.4.3. Raman analysis. Raman spectroscopy studies were performed to understand the quality and crystallinity of carbon (Fig. 6–8).

Two distinct bands were observed for all the catalysts, the D-band at 1336 cm^{-1} and the G-band at 1570 cm^{-1}. The D-band represents either disordered or amorphous carbon and the G-band represents crystalline carbon.[4] From TGA analysis it was confirmed that there is no amorphous carbon deposited on the catalysts (Fig. 5). Hence the intensity ratio I_D/I_G explains the graphitization degree and the crystallinity of the CNTs.[47] The carbon having the lowest I_D/I_G value is having the highest crystallinity. For Ni–Fe catalysts (Fig. 6) we could observe that the I_D/I_G value was lowest for 9Ni–Fe, 4Ni–1Fe, Ni, and 1Ni–2Fe, which showed similar I_D/I_G values (0.829–0.874) and better crystallinity than 2Ni–Fe, 1Ni–1Fe and Fe catalysts with higher I_D/I_G values (0.944–1.26).

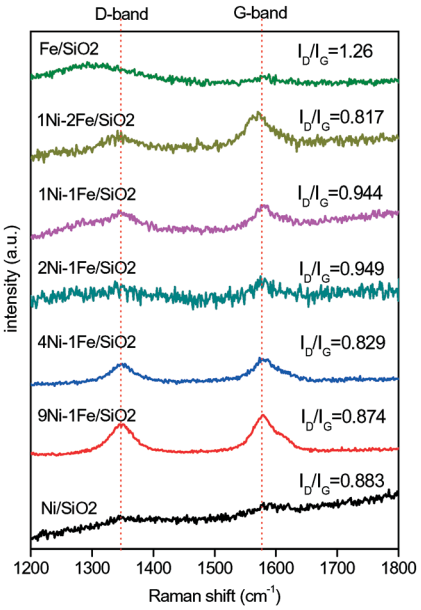

Fig. 6 Raman spectra of CNTs over mono- and bimetallic Ni–Fe catalysts.

Raman spectra for Ni–Co catalysts (Fig. 7) show that 9Ni–1Co gave the most crystalline CNT with the lowest I_D/I_G (0.765), whereas Ni, 4Ni–Co, and 1Ni–1Co showed similar I_D/I_G values (0.868–0.883). We did not observe any distinct bands for Co and 1Ni–9Co catalysts since the amount of CNTs formed for these catalysts was less than the detection limits. The highest crystallinity was calculated for 4Fe–1Co (I_D/I_G = 0.896), whereas Fe, 9Fe–1Co, and 2Fe–1Co showed similar I_D/I_G values (0.983–0.99). Of the remaining catalyst ratios, such as 1Fe–1Co, Fe–2Co and Fe–Co catalysts, 4Fe–1Co

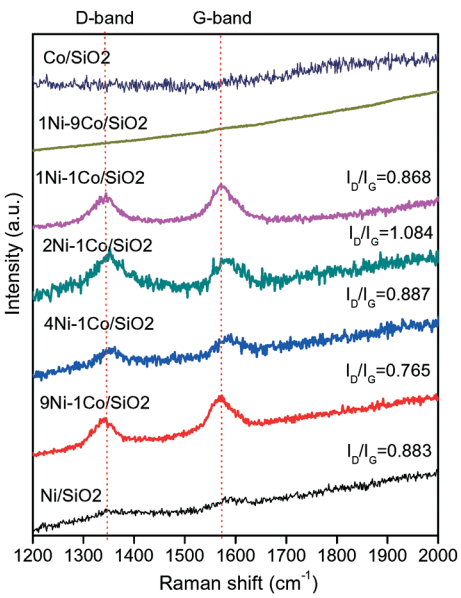

Fig. 7 Raman spectra of CNTs over mono- and bimetallic Ni–Co catalysts.

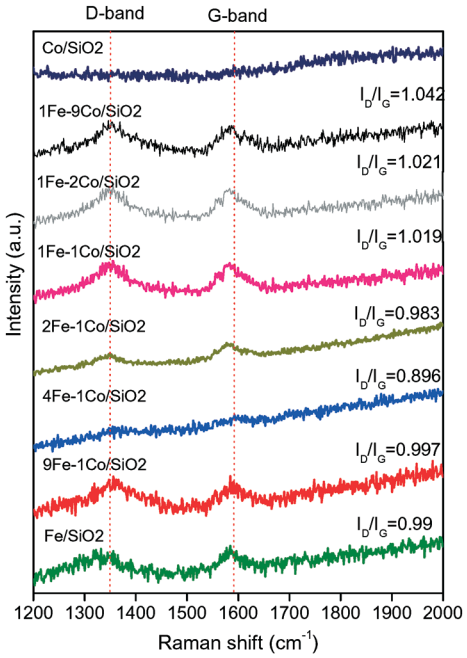

Fig. 8 Raman spectra of CNTs over mono- and bimetallic Fe–Co catalysts.

formed CNT with the highest I_D/I_G (1.019–1042) due to the low crystallinity of the CNT formed.

3.4.4. TEM analysis. The structural morphology, particle size, diameter and growth of CNTs were studied using the TEM technique This analysis was limited to certain catalysts from each set of bimetallic catalysts (Ni–Fe/Ni–Co and Fe–Co) which showed the best performance and stable nature in the methane decomposition reaction (Fig. 9). Hence TEM analysis was performed over the used 9Ni–1Fe/SiO_2, 9Ni–1Co/SiO_2 and 1Fe–2Co/SiO_2 catalysts. It was observed that the CNTs formed in our experiments were found to be MWCNTs due to the large crystallite size of the active site metal nanoparticles, as confirmed by XRD techniques (Table S1, ESI†). The CNTs formed over all these catalysts showed a very crowded dense population with entangled fibres. CNTs were growing in random directions due to the competition for space during growth.[16] The length of the CNT depends on the duration of the process; hence, to obtain longer filaments, the duration of the reaction has to be extended.

For 9Ni–1Fe/SiO_2 catalyst it was observed that most of the CNTs formed were 100–120 nm in size. The wall of the tube was very thick with the graphite layers stacked very closely. Another interesting feature was that when Ni–Fe catalysts were used we could observe a "tip growth" of CNT, where as the CNT grows it takes the metal nanoparticle along with it and is situated at the tip of the CNT. The metal nanoparticle was "cone or pear shaped", tapered towards the end, and forms an angle with the tubular axis. From HR-TEM it was observed that the walls of CNTs formed were of a "fishbone or herringbone" structure in which the graphene layers are stacked obliquely with respect to the fiber axis. In this type of CNT, the graphite planes are formed at an angle to the axis

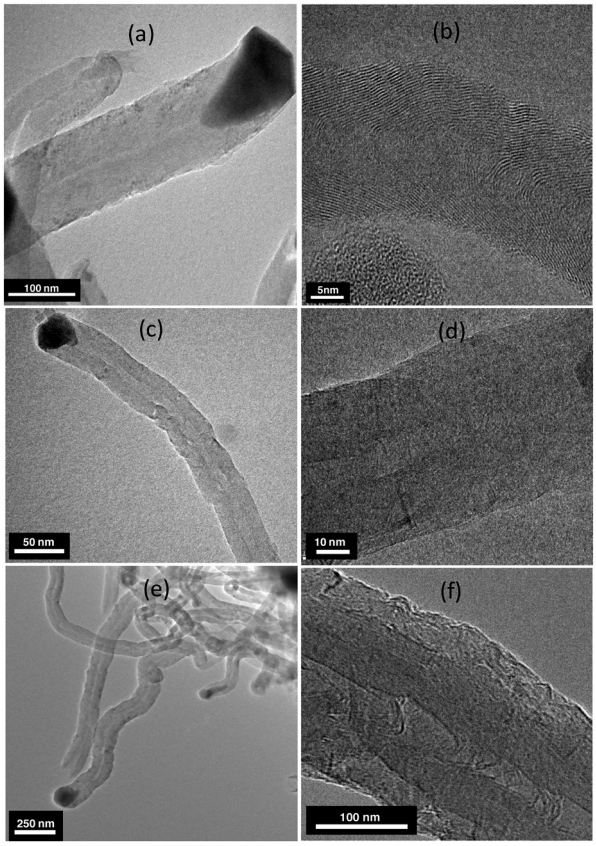

Fig. 9 Growth of carbon filaments over (a and b) 9Ni–1Fe/SiO_2, (c and d) 9Ni–1Co/SiO_2, and (e and f) 1Fe–2Co/SiO_2 catalysts after methane decomposition at T = 650 °C, TOS = 60 minutes, GHSV = 42 000 h^{-1}.

of the nanotube, and hence there is a higher possibility for edge plane sites/defects in these CNTs.[48] For 9Ni–1Co catalyst, MWCNTs with 50–60 nm diameters were formed, also with a metal nanoparticle at the tip. From HR-TEM it was observed that the wall of these CNTs had a parallel morphology (graphite planes arranged parallel to the tubular axis). However, certain fibres formed in these catalysts did not have metal nanoparticles at the tip (Fig. S17, ESI†); the CNT was growing with metal at its base (base growth). Thus, 9Ni–1Co/SiO_2 gave a mixture of tip and base grown CNTs.

In the case of Fe–Co catalyst, once again MWCNTs were formed with diameters of 100–125 nm, also showing a mixture of tip and base grown CNTs (Fig. 9 and S18, ESI†). HR-TEM has confirmed the parallel morphology of the CNT wall for these catalysts.

3.5. Mechanism of tip and base growth of CNTs

There are several models explaining the tip growth mechanism. It was assumed that carbon formed on the surface of the metal nanoparticle diffuses to the back side of the nanoparticle. Still, the driving force which is responsible for the carbon diffusion is not known. For many authors, carbon diffusion was due to the temperature gradient created in the particle due to the exothermic decomposition of methane on

the surface and also the endothermic deposition of carbon on the rear surface.[6,49] It was also explained that due to the lower surface energy of basal planes of graphite compared to prismatic planes, carbon filaments precipitate with the basal planes into a tubular structure.[50] Metal–support interactions have also played an important role in the growth mechanisms of carbon nanotubes. If the metal–support interaction is weak (acute contact angle with the support), methane decomposes on the top surface of the metal and carbon diffuses towards the downside of the metal. The metal particle is squeezed out because of pressure build-up due to the formation of layers of graphite at the interior of the graphitic cap. When the metal is exposed to methane, growth continues until the surface of the metal is covered with excess carbon.

Stronger interaction of metal nanoparticles with support (obtuse angle of metal with the support) facilitates "base growth" of carbon nanotubes.[6] The decomposition of methane and carbon diffusion in the initial stage is similar to that of the tip growth model but the carbon precipitated is unable to push the metal upwards. Hence the precipitated carbon is compelled to emerge from the upper side of the metal (away from the support surface). It is also known from the literature that the high surface energy of the metal nanoparticles is reduced by the deposition of the graphene planes, which are strongly chemisorbed onto the metal surface. A graphitic cap is formed on the metal nanoparticle which is lifted upwards during the further deposition of carbon fragments. Hence we observe a hollow carbon nanotube growing away from the metal nanoparticle, which is still attached to the support, or a base growth of carbon nanotubes.[51]

3.6. Synthesis of base grown CNTs

Based on previous studies we found that Fe-based catalysts generated base grown CNTs. Also from our catalyst screening studies using mono- and bimetallic Ni/Fe/Co catalysts we have understood that 60% Fe/SiO_2 was selectively forming base grown CNTs during methane decomposition. Hence we chose Fe/SiO_2 catalysts for our preliminary work. From our experimental results we understood that Fe/SiO_2 had a very low methane conversion, 11%, and eventually was reduced to 4% at T = 650 °C, TOS = 60 minutes, GHSV = 42 000 h^{-1}. Hence the reaction conditions have to be optimized to obtain better conversion and yields of H_2 and CNT.

The effect of temperature on the base growth of CNT was studied over Fe/SiO_2 catalyst at various temperatures, T = 650, 700, 750 and 800 °C (Fig. 10). It was observed that at T = 750 °C methane conversion was 50%, better than 47% at T = 700 °C, but after 15 min of reaction methane conversion was similar in both cases. Hence T = 700 °C was preferred for future studies.

Base grown CNT formation was confirmed using TEM analysis. It was observed that metal nanoparticles remained on the support, while the CNTs grow from the base (Fig. 11).

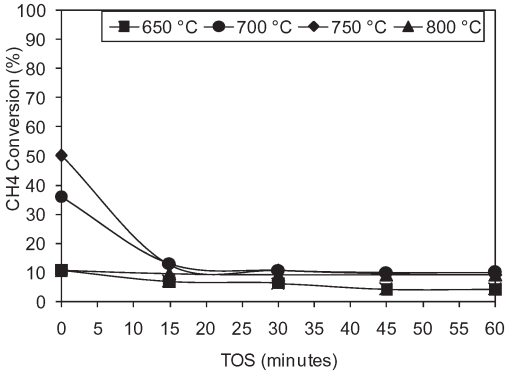

Fig. 10 Base growth of carbon filaments over Fe/SiO_2 catalysts at (a) T = 650 °C and (b) T = 650 °C. TOS = 60 minutes, GHSV = 42 000 h^{-1}.

Hence, 60% Fe/SiO_2 catalyst was proved to be capable of synthesizing base grown CNTs by methane decomposition. We performed a few reactions with GHSV = 21 000 h^{-1} which is half of the value (42 000 h^{-1}) in all our reactions, with a similar catalyst amount (0.1 g) and 30% CH_4/N_2. There was definitely an improvement of 10–15% of CH_4 conversion (Table S3†).

In order to confirm this property of Fe/SiO_2 catalyst we performed a catalyst regeneration study. After the first cycle of methane decomposition at T = 650 °C, TOS = 60 min, and GHSV = 42 000 h^{-1}, the used catalyst was regenerated using 10% O_2 at 500 °C for 30 min. Carbon deposited on the catalyst was burnt off as CO_2 which was confirmed using GC analysis.

The second cycle of experiments was performed under the same reaction conditions (Fig. 12). CNT formed in the 2nd cycle was characterized using TEM which confirmed the formation of base grown CNTs even in the 2nd cycle (Fig. 13). We observed a slight variation in the catalytic activity after regeneration which can be due to sintering of metal particles. Raman analysis of both the 1st and 2nd cycles of CNTs was performed, which showed that in the 2nd cycle the intensity of the D-band corresponding to disordered CNT was higher than that of the G-band corresponding to the crystallinity of the CNT (Fig. 14). Thus, even after a regeneration study the activity of Fe/SiO_2 was not reduced, but the selectivity of this

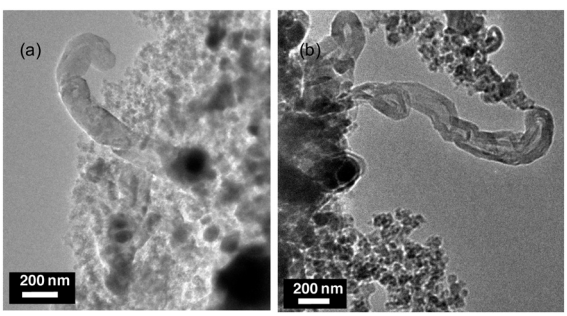

Fig. 11 TEM images (a & b) of base grown carbon nanotubes with Fe/SiO_2 catalysts at T = 700 °C, TOS = 60 minutes, GHSV = 42 000 h^{-1}.

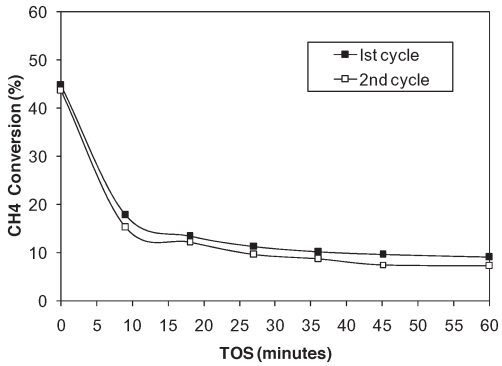

Fig. 12 Catalyst regeneration study over Fe/SiO_2 catalysts at T = 650 °C, TOS = 60 minutes, GHSV = 42 000 h^{-1}.

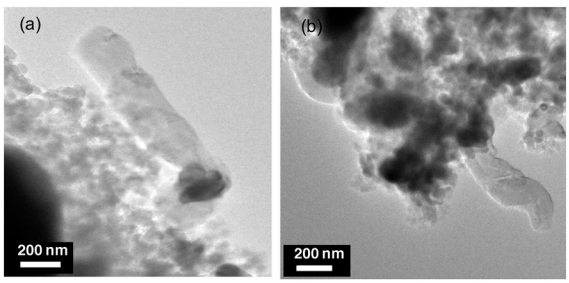

Fig. 13 TEM images (a & b) of base grown carbon nanotubes in the 2nd cycle of Fe/SiO_2 catalysts at T = 700 °C, TOS = 60 minutes, GHSV = 42 000 h^{-1}.

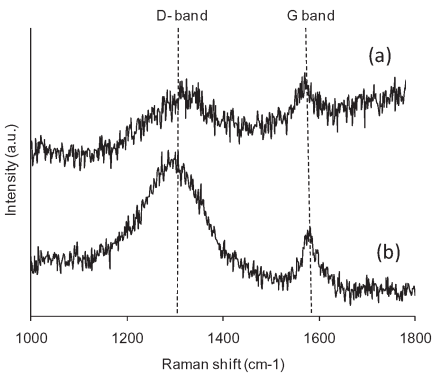

Fig. 14 Raman spectra of base grown carbon nanotubes over Fe/SiO_2 catalysts. (a) Ist cycle and (b) 2nd cycle at T = 700 °C, TOS = 60 minutes, GHSV = 42 000 h^{-1}.

catalyst towards CNT formation was found to decrease after the regeneration study. Hence in order to improve the selectivity of the catalyst towards CNT formation, a more detailed study is required.

Conclusions

The central theme of this project is the catalytic decomposition of methane, the major component of shale gas, into CO_x-free H_2 and valuable carbon such as CNT. However, to attain this goal a thorough investigation of the reaction conditions, catalyst properties and the carbon generated by the process has to be performed.

In summary, the catalytic activity, selectivity and stability of mono- and bimetallic Ni/Fe/Co based catalysts were demonstrated for the methane decomposition study. The novelty in our work is that we investigated the performance of transition metal catalysts (Ni/Fe/Co) for the synthesis of both tip and base grown CNTs by methane decomposition. We have synthesized mono- and bimetallic Ni/Fe/Co catalysts with 60 wt% metal loading by dry impregnation over a SiO_2 support. XRD analysis showed that the crystallite size of bimetallic catalysts was found to be smaller than that of the monometallic ones, which corresponds to an increase in the number of active sites in the bimetallic catalysts. This can be one of the reasons for the higher activity of the bimetallic catalysts compared to monometallic ones. The reason for the higher stability of bimetallic catalysts can be due to alloy formation, which results in structural and electronic rearrangements and the formation of small nanoparticles which can prevent their agglomeration and retain the stability of the catalysts. XRD and H_2-TPR analysis confirmed the formation of the alloy in the bimetallic catalysts. The effect of catalyst composition on methane decomposition and CNT growth was studied over various mole ratios of Ni-, Fe- and Co-based catalysts. The Ni–Fe bimetallic catalysts with high Ni content exhibited higher methane conversion and also contributed to the increase in the stability of the catalyst. In the case of Ni–Co bimetallic catalysts, those with a higher Ni content exhibited higher conversion, and Co present in the catalyst contributed to the increase in the catalyst lifetime. Among Fe–Co catalysts the activity towards methane conversion was comparatively lower than that of Ni–Fe and Ni–Co catalysts. The quality of the CNTs formed over these catalysts was analysed using XRD, TGA, Raman and TEM techniques. From XRD analysis it was understood that the Ni content in the bimetallic catalyst controls the degree of graphitization of the carbon formed. From TGA analysis it was concluded that there was no amorphous carbon formation during methane decomposition over these catalysts. The quality of the carbon, that is, the degree of crystallinity, was calculated using Raman analysis. TEM analysis helped to understand the different morphologies of the CNT, diameter, wall type (parallel or fishbone type) and also the growth mechanism such as tip and base growth on different catalysts. It was understood that Ni–Fe catalysts selectively produced tip grown CNTs with a fishbone wall pattern, whereas Ni–Co and Fe–Co catalysts formed a mixture of tip and base grown CNTs with a parallel wall pattern.

Previous catalytic studies on methane decomposition were mainly focussed on these metals individually as catalysts for CNT formation and hydrogen production. Also there was a lack of information about the relation between the type of metal and the properties of CNTs formed during methane decomposition. Our work is indeed significantly more general using a variety of combinations of Ni/Fe/Co catalysts under

the same reaction conditions for methane decomposition. We have explored and selectively synthesised base grown CNTs over Fe/SiO_2, which are considered to be easily harvested without sacrificing the catalyst sites. Therefore this work opens new opportunities and a new frontier for synthesis of CNTs and CO_x-free H_2 by the catalytic decomposition of methane.

Conflicts of interest

There are no conflicts to declare.

Acknowledgements

The authors acknowledge financial support from WVU Research Corporation and WVU Benjamin M. Statler College of Engineering and Mineral Resources.

References

1 J. Holladay, J. Hu, D. King and Y. Wang, *Catal. Today*, 2009, **139**, 244–260.
2 R. W. Howarth, *Energy Sci. Eng.*, 2014, **2**, 47–60.
3 J. N. Armor, *Appl. Catal., A*, 1999, **176**, 159–176.
4 Q. Weizhong, L. Tang, W. Zhanwen, W. Fei, L. Zhifei, L. Guohua and L. Yongdan, *Appl. Catal., A*, 2004, **260**, 223–228.
5 G. E. Gadd, M. Blackford, S. Moricca, N. Webb, P. J. Evans, A. M. Smith, G. Jacobsen, S. Leung, A. Day and Q. Hua, *Science*, 1997, **277**, 933–936.
6 R. T. K. Baker, *Carbon*, 1989, **27**, 315–323.
7 P. Chen, X. Wu, J. Lin and K. L. Tan, *Science*, 1999, **285**, 91–93.
8 N. M. Rodriguez, M.-S. Kim and R. T. K. Baker, *J. Phys. Chem.*, 1994, **98**, 13108–13111.
9 K. P. D. E. Jong and J. W. Geus, *Catal. Rev.: Sci. Eng.*, 2000, **42**, 481–510.
10 H. F. Abbas and W. M. A. W. Daud, *Int. J. Hydrogen Energy*, 2010, **35**, 1160–1190.
11 T. V. Choudhary and D. W. Goodman, *Analysis*, 2006, **19**, 164–183.
12 T. Zhang and M. D. Amiridis, *Appl. Catal., A*, 1998, **167**, 161–172.
13 A. M. Amin, E. Croiset and W. Epling, *Int. J. Hydrogen Energy*, 2011, **36**, 2904–2935.
14 S. T. Hussain, S. Gul, M. Mazhar, D. H. Anjum and F. Larachi, *J. Nat. Gas Chem.*, 2008, **17**, 374–382.
15 Y. Wang, J. Peng, C. Zhou, Z.-Y. Lim, C. Wu, S. Ye and W. G. Wang, *Int. J. Hydrogen Energy*, 2014, **39**, 778–787.
16 G. Wang, Y. Jin, G. Liu and Y. Li, *Energy Fuels*, 2013, **27**, 4448–4456.
17 Y. Li, J. Chen, Y. Ma, J. Zhao, Y. Qin and L. Chang, *Chem. Commun.*, 1999, 1141–1142.
18 J. Chen, Y. Li, Z. Li and X. Zhang, *Appl. Catal., A*, 2004, **269**, 179–186.
19 I. Suelves, M. J. Lázaro, R. Moliner, Y. Echegoyen and J. M. Palacios, *Catal. Today*, 2006, **116**, 271–280.
20 J. Ashok, P. S. Reddy, G. Raju, M. Subrahmanyam and A. Venugopal, *Energy Fuels*, 2009, **23**, 5–13.
21 A. Monzón, N. Latorre, T. Ubieto, C. Royo, E. Romeo, J. I. Villacampa, L. Dussault, J. C. Dupin, C. Guimon and M. Montioux, *Catal. Today*, 2006, **116**, 264–270.
22 M. A. Ermakova, D. Y. Ermakov and G. G. Kuvshinov, *Appl. Catal., A*, 2000, **201**, 61–70.
23 A. E. Awadallah, M. S. Abdel-Mottaleb, A. A. Aboul-Enein, M. M. Yonis and A. K. Aboul-Gheit, *Chem. Eng. Commun.*, 2015, **202**, 163–174.
24 L. B. Avdeeva, T. V. Reshetenko, Z. R. Ismagilov and V. A. Likholobov, *Appl. Catal., A*, 2002, **228**, 53–63.
25 A. H. Fakeeha, A. A. Ibrahim, W. U. Khan, A. E. Abasaeed and A. S. Al-Fatesh, *Pet. Sci. Technol.*, 2016, **34**, 1617–1623.
26 W.-H. Chiang and R. M. Sankaran, *Adv. Mater.*, 2008, **20**, 4857–4861.
27 W.-Q. Deng, X. Xu and W. A. Goddard, *Nano Lett.*, 2004, **4**, 2331–2335.
28 W. Shen, Y. Wang, X. Shi, N. Shah, F. Huggins, S. Bollineni, M. Seehra and G. Huffman, *Energy Fuels*, 2007, **21**, 3520–3529.
29 M. Pudukudy, Z. Yaakob and Z. S. Akmal, *Appl. Surf. Sci.*, 2015, **330**, 418–430.
30 S. A. Shokry, A. K. El Morsi, M. S. Sabaa, R. R. Mohamed and H. E. El Sorogy, *Egypt. J. Pet.*, 2014, **23**, 183–189.
31 H. Yoshida, S. Takeda, T. Uchiyama, H. Kohno and Y. Homma, *Nano Lett.*, 2008, **8**, 2082–2086.
32 J. Li, C. Papadopoulos, J. M. Xu and M. Moskovits, *Appl. Phys. Lett.*, 1999, **75**, 367–369.
33 S. Hofmann, R. Sharma, C. Ducati, G. Du, C. Mattevi, C. Cepek, M. Cantoro, S. Pisana, A. Parvez, F. Cervantes-Sodi, A. C. Ferrari, R. Dunin-Borkowski, S. Lizzit, L. Petaccia, A. Goldoni and J. Robertson, *Nano Lett.*, 2007, **7**, 602–608.
34 S. Fan, M. G. Chapline, N. R. Franklin, T. W. Tombler, A. M. Cassell and H. Dai, *Science*, 1999, **283**, 512–514.
35 L.-H. Zhu, X.-M. Ma and L. Zhao, *J. Mater. Sci.*, 2001, **36**, 5571–5574.
36 J. F. Valderruten, G. A. P. Alcázar and J. M. Grenèche, *J. Phys.: Condens. Matter*, 2008, **20**, 485204.
37 N. Wang, W. Chu, T. Zhang and X. S. Zhao, *Int. J. Hydrogen Energy*, 2012, **37**, 19–30.
38 P. Ubilla, R. Garcia, J. L. G. Fierro and N. Escalona, *J. Chil. Chem. Soc.*, 2010, **55**, 35–38.
39 J. Yang, Y. Sun, Y. Tang, Y. Liu, H. Wang, L. Tian, H. Wang, Z. Zhang, H. Xiang and Y. Li, *J. Mol. Catal. A: Chem.*, 2006, **245**, 26–36.
40 P. Jana, V. A. de la Peña O'Shea, J. M. Coronado and D. P. Serrano, *Int. J. Hydrogen Energy*, 2012, **37**, 7034–7041.
41 D. J. Duvenhage and N. J. Coville, *Appl. Catal., A*, 1997, **153**, 43–67.
42 R. J. Kaleńczuk, *Catal. Lett.*, 1995, **33**, 255–268.
43 W. Qian, T. Liu, F. Wei, Z. Wang and Y. Li, *Appl. Catal., A*, 2004, **258**, 121–124.
44 W. Z. Zhu, D. E. Miser, W. G. Chan and M. R. Hajaligol, *Mater. Chem. Phys.*, 2003, **82**, 638–647.

45 C.-M. Chen, Y.-M. Dai, J. G. Huang and J.-M. Jehng, *Carbon*, 2006, **44**, 1808–1820.
46 A. E. Awadallah, M. S. Abdel-Mottaleb, A. A. Aboul-Enein, M. M. Yonis and A. K. Aboul-Gheit, *Chem. Eng. Commun.*, 2015, **202**, 163–174.
47 A. E. Awadallah, A. A. Aboul-Enein, D. S. El-Desouki and A. K. Aboul-Gheit, *Appl. Surf. Sci.*, 2014, **296**, 100–107.
48 C. E. Banks and R. G. Compton, *Analyst*, 2006, **131**, 15–21.
49 H. Kanzow and A. Ding, *Phys. Rev. B: Condens. Matter Mater. Phys.*, 1999, **60**, 11180–11186.
50 G. G. Tibbetts, *J. Cryst. Growth*, 1984, **66**, 632–638.
51 H. Dai, A. G. Rinzler, P. Nikolaev, A. Thess, D. T. Colbert and R. E. Smalley, *Chem. Phys. Lett.*, 1996, **260**, 471–475.